The relationship of water isotopes to orographic precipitation and regional climate

Astrid Pacini

Advisor: Mark Brandon
Second Reader: Ronald Smith

Friday May 6, 2016

A Senior Thesis presented to the faculty of the Department of Geology and Geophysics, Yale University, in partial fulfillment of the Bachelor's Degree.

Abstract

Orographic precipitation occurs when moist air travels across topography and is lifted. This lifting generates condensation and the precipitation promotes isotopic fractionation. This means that as the air parcel moves over the topography from the windward to leeward side of the range, the isotopic content of the water becomes increasingly lighter, as the heavy isotopes precipitate out preferentially. Therefore, the isotopic composition of a water sample can give insight into the topography the parcel encountered and its associated pattern of precipitation. The goal of this work is to look at stable isotopes in meteoric water as a means to estimate climate parameters for Patagonia. This work, after briefly presenting the existing numerical scheme of the linear theory of orographic precipitation (Smith and Barstad, 2004), will examine three aspects and outcomes of this scheme. Firstly, it will look at how the model estimates physical parameters. Secondly, the physical parameters will be shown to be reasonable and consistent with climatological values. Thirdly, this work will present a comparison of the output isotopic values of the model with observed values. With a functional model, with best-fit climate parameters, the model can then be inverted and, inputting isotopic values, we can obtain topographic measures. This inversion will permit measurement of paleo-topography given paleo-isotopic values, as measured through hydrogen in volcanic glasses.

Table of Contents

1. Introduction

When an air mass carrying moisture is forced to lift over topography, pressure decreases, water vapor condenses, and liquid water rains out (Wallace and Hobbs, 2006), as seen schematically in Figure 1. Water molecules containing ^{2}H or ^{18}O preferentially condensate over ^{1}H or ^{16}O-containing vapor, leaving the remaining body of moisture isotopically lighter, or depleted in heavy isotopes (Criss, 1999, p. 18). This produces a rain shadow on the downwind side of the topographic barrier. The higher the topographic barrier, the greater the degree of rain out and thus the more depleted the isotopes in precipitation downstream will be (Poage and Chamberlin, 2001).

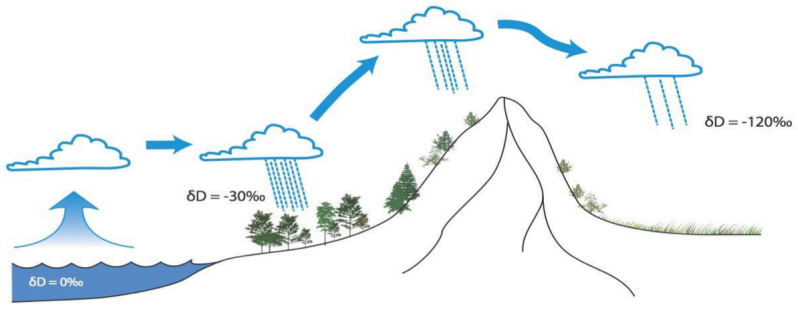

Figure 1. Orographic precipitation and the Rayleigh effect. Source Auerbach 2015.

There has been significant interest in attempting to use fractionation of water isotopes to infer the size of topography in the past (Rowley and Garzione, 2007). Almost all interpretations at present are based on a one-dimensional lifting model. However, there are problems associated with this model, as one-dimensional lifting only examines the evanescent case (discussed in more depth in section 2.3) and does not account for the effects of backing and propagation upstream (Smith, 1979; Smith and Barstad, 2004). The linear model provides a way of looking at these excluded characteristics (Smith and Barstad, 2004).

Herein we present the theory for orographic precipitation and isotopic fractionation and briefly describe a published numerical scheme. This is used to find a best-fit solution for a small set of climate parameters (wind speed, azimuth, sea-level temperature, moist Brunt-Väisälä, τ (condensation and fall out times), and background precipitation) which are fit against 233 water isotope values from the Patagonian Andes (Stern and Blisniuk, 2002; Smith and Evans, 2007).

This region was chosen due to the constant presence of westerly winds, as shown in the wind rose in Figure 2. This means that the moisture in the atmosphere comes from the isotopically stable and consistent source of Pacific-origin moisture. This allows us to calibrate the model and to run its inverse. We can feed the model values of downstream paleo-isotopic composition as obtained from volcanic glasses and it will report on the paleo-topography that these isotopes encountered such that they were depleted to their given composition, given their geographic location.

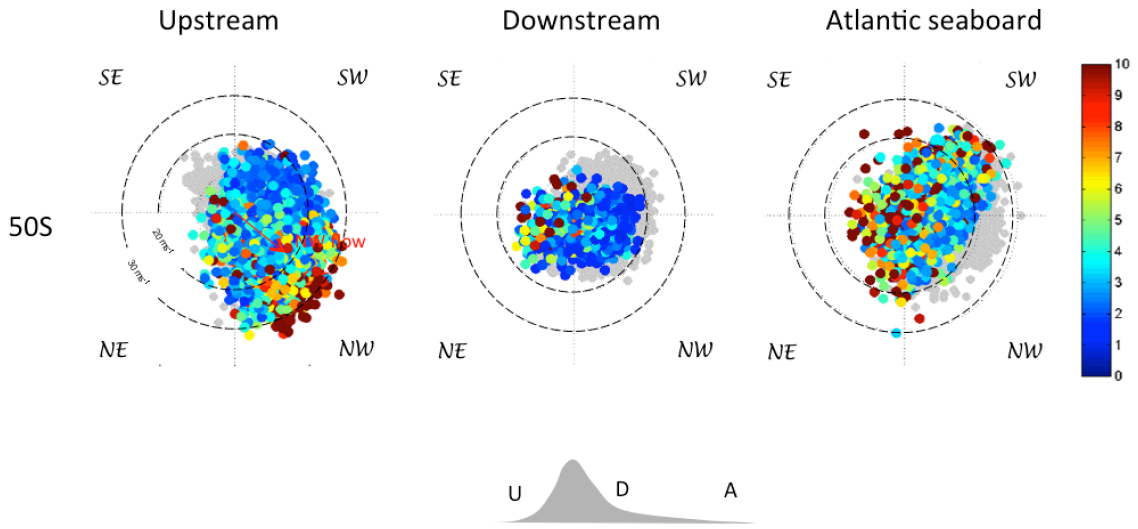

Figure 2. Wind rose schematic for upstream, downstream, and the Atlantic seaboard at 50°S at 850 hPa (~1500 m altitude) (this study uses an average latitude of 46.4°S). The grey values represent all days, the colored values represent days with precipitation and are shaded according to this precipitation. Note that the coordinate system is oriented such that values in each corner represent the direction that the flow is moving towards. In other words, values in the bottom right corner represent NW flow (from NW to SE), while values in the top left represent SE flow (from SE to NW). The contours represent wind speeds of 20 m/s and 30 m/s. Notably, the upstream region experiences high amounts of NW flow at high velocities, emphasizing that most of the moisture in orographic precipitation is coming from the stable source of Pacific water. From Garreaud, Presentation, April 26, 2016.

2. Background

2.1 Precipitation

In general, three different atmospheric dynamics can cause precipitation. Precipitation is seen in synoptic events, such as extratropical cyclones, with large length scales O(~1000km) that penetrate high into the atmosphere and exhibit large fractionation over a large geographical

region (Wallace and Hobbs, 2006). They are generated by an air mass rising above another and thus forcing condensation (Wallace and Hobbs, 2006). Precipitation is also seen in convective instabilities and the associated lifting of air parcels. This lifting again causes condensation and thus precipitation (Wallace and Hobbs, 2006). Of interest to this study is the third mechanism—topography. As aforementioned, when an air parcel encounters topography, it is lifted and adiabatically expands. Condensation forms and precipitation occurs from the release of latent heat of condensation (Wallace and Hobbs, 2006). This effect can be modeled from a governing set of equations and perturbations around a mean flow. Therefore, there are three main mechanisms that cause precipitation, and only one of these three is due to topography.

2.2 Underlying Equations

Imagine a flow of air with horizontal velocity $\vec{U} = u\hat{\imath} + v\hat{\jmath}$ over a topography of *h(x,y)* such that it is fully saturated. The wind can be broken down into its $u = u(x,y,z)$, $v = v(x,y,z)$, and $w = w(x,y,z)$ components and the coordinate frame orients the positive *x* direction with the wind and positive *z* direction with the vertical orientation above topography. We break down the velocity equations into a mean state and a linear perturbation such that

$$u(x,y,z) \approx \bar{u} + u'(x,y,z) \tag{1}$$

$$v(x,y,z) \approx \bar{v} + v'(x,y,z) \tag{2}$$

$$w(x,y,z) \approx w'(x,y,z) \tag{3}$$

with the mean state denoted by – and the perturbation denoted by $'$ (Lin, 2007, p.14). The wind field is assumed to be adiabatic and follow the Boussinesq approximation.

We define five fundamental equations (momentum in three directions, continuity, and thermodynamic equation) such that,

$$\bar{u}\frac{\partial u'}{\partial x} + \bar{v}\frac{\partial u'}{\partial y} - fv' + \frac{1}{\bar{\rho}}\frac{\partial P'}{\partial x} = 0 \tag{4}$$

$$\bar{u}\frac{\partial v'}{\partial x} + \bar{v}\frac{\partial v'}{\partial y} + fu' + \frac{1}{\bar{\rho}}\frac{\partial P'}{\partial y} = 0 \tag{5}$$

$$\bar{u}\frac{\partial w'}{\partial x} + \bar{v}\frac{\partial w'}{\partial y} - \frac{g}{\bar{\theta}}\theta' + \frac{1}{\bar{\rho}}\frac{\partial P'}{\partial z} = 0 \tag{6}$$

$$\frac{\partial u'}{\partial x}+\frac{\partial v'}{\partial y}+\frac{\partial w'}{\partial z}=0 \tag{7}$$

$$\bar{u}\frac{\partial \theta'}{\partial x}+\bar{v}\frac{\partial \theta'}{\partial y}+\frac{\bar{\theta}N_m^2}{g}w'=0 \tag{8}$$

where again – represents the mean state and $'$ represents perturbations to this mean state (Lin, 2007, p. 15-16). P represents the pressure, f the Coriolis force, and θ the potential temperature. We have assumed a vertical velocity in the mean state in the z-direction to be zero and have assumed time invariant perturbations (Lin, 2012, p. 15).

We use 2-dimensional Fourier transformations to obtain solutions in the wave domain for h, u, v, and w (Smith, 1980). The initial transformation used is shown

$$\hat{\phi}(k,l)=\int_{-\infty}^{+\infty}\int \phi(x,y)e^{-i(kx+ly)}\,\mathrm{d}x\,\mathrm{d}y \tag{9}$$

which MATLAB renders with the fft2 command and where $\hat{\phi}$ represents the solution in the wave domain, and k and l represent the wind components in parallel and perpendicular to the wave number vector respectively (Smith et al., 2005; Smith and Evans, 2007). k and l are defined as

$$k_{n_k}=k=2\pi\frac{n_k-1}{\Delta_x N_x}, \tag{10}$$

$$l_{n_l}=l=2\pi\frac{n_l-1}{\Delta_y N_y}, \tag{11}$$

where the Δ_x and Δ_y indicate the spacing of the nodes in the x and y directions in the space domain and n_x and n_y indicate indices from 1 to N_x and N_y respectively (Brown, 1963).

The following inverse Fourier transformation yields

$$\phi(x,y)=\mathrm{Re}\left\{(2\pi)^{-2}\int_{-\infty}^{+\infty}\int \hat{\phi}(k,l)e^{i(kx+ly)}\,\mathrm{d}k\,\mathrm{d}l\right\} \tag{12}$$

such that we can convert back from the wave domain to the spatial domain, which in MATLAB is performed with the ifft2 command (Smith and Evans, 2007).

We are particularly interested in the vertical velocity, as that determines the lifting a given parcel experiences and thus the condensation and ultimately the fractionation that the parcel exhibits. The vertical velocity is represented by the following expression in the wave domain,

$$\hat{w}(k,l,z) = i\sigma e^{imz}\hat{h}(k,l) \tag{13}$$

where,

$$\sigma = uk + vl \tag{14}$$

with σ representing the intrinsic frequency and m the vertical wavenumber (Nappo, 2012). The vertical wave number m is defined as

$$m^2 = k_H^2\left[\frac{N_m^2 - \sigma^2}{\sigma^2 - f^2}\right] \tag{15}$$

such that

$$k_H^2 = k^2 + l^2 \tag{16}$$

where k_H represents the horizontal wave number (Smith et al., 2005; Smith and Evans, 2007), f represents the Coriolis frequency ($f = 2\Omega\sin\phi$, where Ω is the rotation rate of the Earth, 7.2921 $\times$ 10^{-5} rad/s, and ϕ is the latitude (Wallace and Hobbs, 2006)) and N_m represents the stability. The uk value indicates the oscillation frequency of the flow over the given topography. The Coriolis correction is unnecessary if the region is horizontally less than 100 m to 100 km, therefore we disregard f (Smith and Barstad, 2004; Nappo, 2012). The vertical wave number thus indicates frequency of the induced mountain waves in the vertical direction spatially. If s is defined as the wind path and $x = s$, then $v = 0$ and $l = 0$. Thus (15) becomes

$$m = \sqrt{\frac{N_m^2}{U^2} - k^2}\ . \tag{17}$$

In addition to the Fourier solution for the vertical velocity, we solve for the horizontal perturbation components according to the vertical velocity by using equation 9 to find $\hat{h}$ and subsequently using equation 13 to find $\hat{w}$ such that we can then solve for $\hat{u}$ and $\hat{v}$ according to

$$\hat{u}(k,l,z) = im\left(\frac{ik + fl/\sigma}{k_H^2}\right)\hat{w}(k,l,z), \tag{18}$$

$$\hat{v}(k,l,z) = im\left(\frac{il - fk/\sigma}{k_H^2}\right)\hat{w}(k,l,z), \tag{19}$$

Therefore, from the fundamental five equations (4-8) and using the Boussinesq approximation along with Fourier transformations to and from the wave domain, we obtain a solution in the spatial domain. In particular, we define the flow-field and streamlines shown in Figure 3 according to the best-fit parameters calculated in Section 3.2.

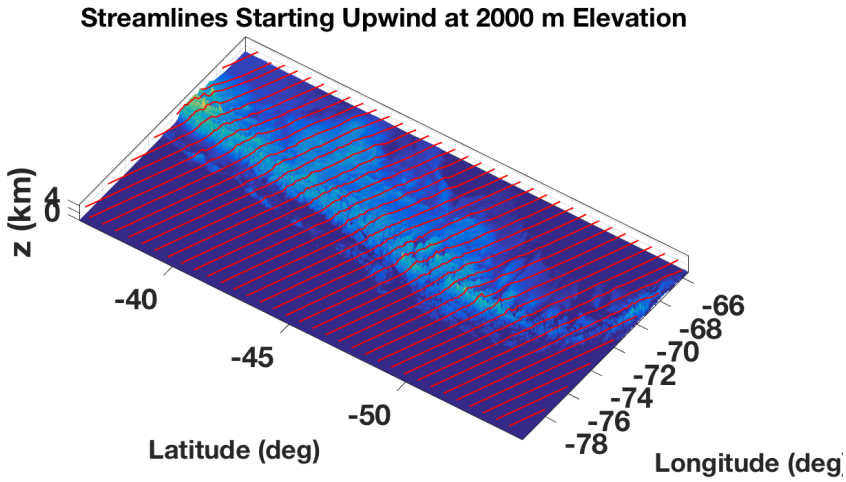

Figure 3. Streamlines over topography in Southern South America. Streamlines were calculated based on best-fit parameters obtained as described in Section 3.2.

2.3 Mountain Waves

As mentioned, as an air mass moves over topography, it is lifted according to the stability of the atmosphere. This stability is dictated by the Brunt-Väisälä frequency,

$$N_m = \sqrt{-\frac{g}{\rho}\frac{\partial \rho}{\partial z}} = \sqrt{-g\frac{\partial \ln \rho}{\partial z}} \approx \sqrt{\frac{g}{T}\left(\Gamma_m - \gamma\right)} \tag{20}$$

where Γ_m represents the moist adiabatic lapse rate and γ represents the environmental lapse rate, g is the gravitational acceleration and ρ is the density (Durran and Klemp, 1982). We have assumed that the model exhibits uniform moist stability. The wave regime then depends on the stratification, oscillation frequency, and vertical wavenumber such that if N_m is zero, we have the neutrally buoyant case where waves are in line with the topography and do not decay in the vertical (Figure 4). Subsequently, a strong topographic perturbation in comparison to the stability of the atmosphere creates the evanescent case, where we have wave fronts that are aligned but

decay in the vertical with 1/m. As N_m increases, upstream phase tilt begins to occur, and then blocking (Figure 4) (Nappo, 2012, 66-67).

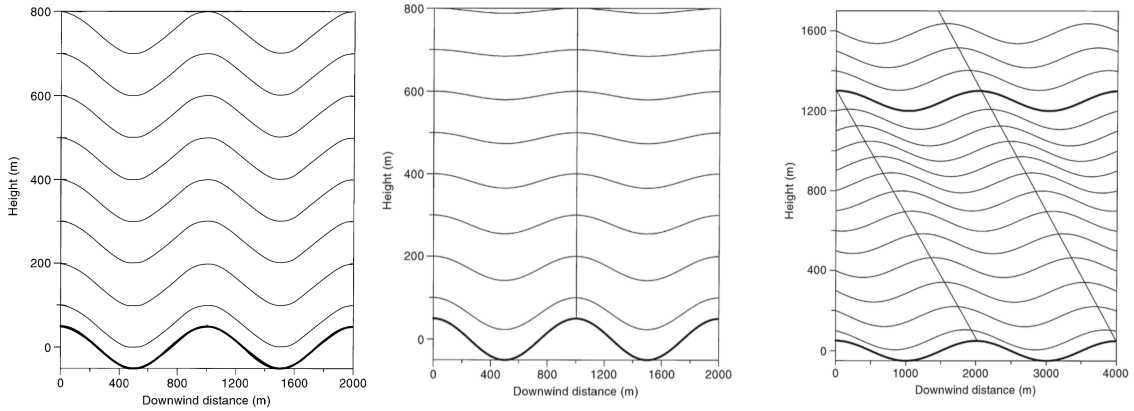

Figure 4. Neutrally buoyant waves over topography (left). Evanescent waves over topography (center). Upstream tilting over topography (right). Increasing N_m from left (N_m = 0) to right. Modified from Nappo, 2012 66-67.

2.4 Isotope Fractionation

Preferential isotopic fractionation over topography is known as the Rayleigh effect. This Rayleigh fractionation is governed by

$$\frac{dR_v}{R_v} = \left(\alpha(T) - 1\right)\frac{\mathrm{d}F}{F}, \text{ and} \tag{21}$$

$$R_p = \alpha(T) R_v . \tag{22}$$

where R_v is the mass ratio for the isotopes (^{2}H/^{1}H or ^{18}O/^{16}O) in the vapor phase and R_p is the mass ratio for the isotopes in the liquid phase (Criss, 1999, p. 106-108). α is the isotope fractionation factor defined as

$$\alpha = \frac{R_p}{R_v} = (\delta^{18}O_p + 1000)/(\delta^{18}O_v + 1000) \tag{23}$$

where,

$$\delta^2 O_p = \left(\frac{R_p}{R_{SMOW}} - 1\right) * 1000 \tag{24}$$

where SMOW stands for standard mean ocean water (Rowley and Garzione, 2007). This same relationship is also applicable for ^{2}H/^{1}H fractionation (Rowley and Garzione, 2007).

The water vapor flux F(x,y) is defined as

$$F(x,y) = U\int_0^\infty \rho_{sh}(x,y)\, e^{-z/H_w}\, \mathrm{d}z = UH_w\rho_{sh}(x,y) \tag{25}$$

where U is the horizontal velocity and H_w the characteristic height for decay of water vapor density from the surface, increasing with altitude, and $\rho_{sh}(x,y)$ represents water vapor density structure (Smith and Evans, 2007). Logically, the precipitation rate [M/L^{2}T] is defined as

$$P(x,y) = -\frac{\partial F(x,y)}{\partial x} = -UH_w \frac{\partial \rho_{sh}(x,y)}{\partial x} \tag{26}$$

We introduce the concept of reduced precipitation (Smith and Evans, 2007), which examines the relative amount of water vapor lost to the total water vapor,

$$r_p(x,y) = \frac{\rho_{s0}}{\rho_{sh}(x,y)} P(x,y) \tag{27}$$

where ρ_{s0} is the saturated water vapor density at sea level. Therefore, substituting equation 26 into 27, we obtain

$$r_{p,\max}(x,y)\mathrm{d}x = -UH_w\rho_{s0} / \rho_{sh} \ \frac{\partial \rho_{sh}(x,y)}{\partial x} = -UH_w\rho_{s0}\mathrm{d}\ln\rho_{sh}(x,y) \tag{28}$$

We take only the positive values, as denoted by the max subscript (Smith and Barstad, 2004) and can thus compute the changes in water vapor flux $F(x,y)$ by substituting equation 28 into equation 26 such that

$$\frac{\partial F(x,y)}{\partial x} = UH_w \frac{\partial \rho_{sh}(x,y)}{\partial x} = -\frac{\rho_{sh}(x,y)}{\rho_{s0}} r_{p,max}(x,y) \tag{29}$$

and further reduction produces

$$\frac{\mathrm{d}F(x,y)}{F(x,y)} = -\frac{r_{p,max}(x,y)}{UH_w\rho_{s0}}\mathrm{d}x\,. \tag{30}$$

Therefore, we have solved for the water vapor flux field, the precipitation field, and the reduced precipitation field according to ρ_{sh} and ρ_{s0}, U, and H_w.

Heavy isotopes are preferentially precipitated out in a lifting-scenario atmosphere, where condensation allows for this precipitation. In particular, the model does not make any assumptions about upstream isotopic content but does utilize the temperature field. Notably, the isotopic fractionation depends only on the reduced, or relative, precipitation, not the precipitation as a whole.

3. Results

3.1 Water data

As mentioned, Patagonia lies in the zone of predominant Westerlies, as seen in Figure 2. Over the field season from December 2014 to January 2015, 54 water samples were collected in the Patagonia region and these samples have been analyzed for isotopic content on a mass spectrometer. The samples were collected from streams that exhibited rainwater characteristics; we sought sample locations where the streams were flowing steadily enough not to be experiencing significant evaporation but did not exhibit too strong or large a flow such that they were coming from nearby snow or ice sheet melt. These samples were obtained from the point of highest flow in the given stream, and sealed in test tubes with lid and secured with Parafilm. We then extracted subsamples and these were sent to the Stable Isotope Facility at the University of Wyoming to be run on the Picarro L2130-I liquid water analyzer mass spectrometer to obtain isotope values. These samples are combined with values collected by Smith and Evans in 2007 and Stern and Blisniuk in 2002. The isotopic values for all datasets are detailed in Appendix 1 along with the GPS coordinates and elevation of each sample location. For the purposes of this study, only paired data was utilized, meaning that only samples that had both a hydrogen and oxygen reading were considered. Only 3 values were excluded for this reason, as they each lacked a δ^2H value. These samples are plotted geographically in Figure 6, as shown by the grey points.

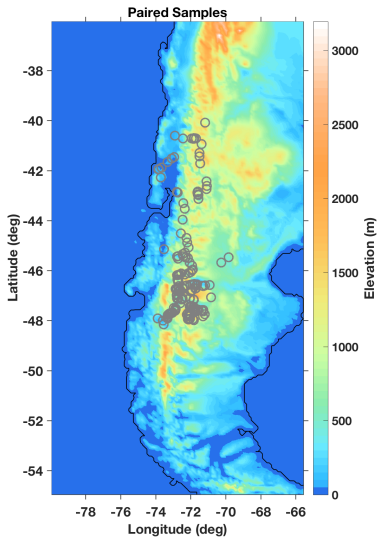

Figure 5. Sample sites for all data. Data are marked by grey points.

The Global Meteoric Water Line is defined as

$$\delta^2 H = 8\times(\delta^{18} O) + 10 \quad (31)$$

and almost all water follows this line unless it has experienced evaporation or other modification (Craig, 1961). As seen in Figure 6, all samples fell generally along this meteoric water line with a correlation of 0.91093 to a slope of 8.11.

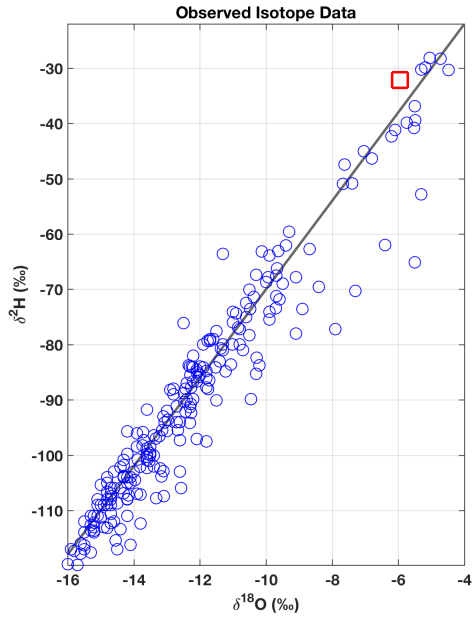

Figure 6. All samples plotted in δ^2H vs. δ^{18}O space, with the global meteoric water line (GMWL) overlain in black. Note that the global meteoric water line is not the best linear fit to this data. However, the data has a slope of 8.11 and an R^2 value of 0.91093.

3.2 Mean State

We find a best-fit value using controlled random search and traditional nonlinear least-square fitting. We perform a grid search across the domain to find the lowest minimum (smallest error), at which point we implement the nonlinear least-square algorithm.

The nonlinear least-square fitting algorithm solves according to the fundamental function that uses residuals

$$r_i = \delta_i - \hat{\delta}_i \quad (32)$$

where *r* represents the residual and the ^ represents the predicted value, while no superscript indicates the observed value. We then examine the squares of the residuals

$$\tilde{S} = S(r_i; \theta_j) = \sum (r_i)^2 |_{\tilde{\theta}_j} \quad (33)$$

for j = 1:J such that ~ represents the candidate solution and θ the parameter. This method is used on the six free parameters in the model:

$$\theta_j = \begin{cases} Wind\ speed \\ Azimuth \\ Sea\ level\ temperature \\ Moist\ Brunt\ Väisälä \\ \tau\ (condensation\ and\ fall\ out\ times) \\ Background\ precipitation \end{cases}$$

We seek to minimize the function $\tilde{S}$ such that

$$\hat{S} = \min S(r_i; \widehat{\theta_j}) \quad (34)$$

where the ^ indicates the best estimate. We calculate

$$\hat{\sigma}^2(r_i) = \hat{S}/(n - m) \quad (35)$$

where *n* represents the number of samples and *m* represents the number of parameters. We calculate an R^2 value according to

$$R^2 = 1 - (\hat{\sigma}^2(r_i)/VAR(r_i)) \quad (36)$$

where

$$VAR(r_i) = \sum (r_i - \bar{r}_i)/n \quad (37)$$

with $mean(r_i) = \bar{r}_i$ (Hansen et al., 2012).

Therefore, the R^2 value looks at the variance of the model relative to the variance of the data. Combining the controlled random search with this nonlinear least-squares algorithm, embedded in the lsqnonlin MATLAB command, we obtain best-fit values for the 6 free parameters listed previously, as seen in Table 1.

All values appear reasonable and consistent with observed parameters with the exception of perhaps the wind speed. A value of 28.6 m/s is extremely high. However, Figure 2 suggests that the majority of precipitation in this region occurs at 30 m/s, so the estimated wind speed could be accurate. The azimuth represents flow from the North West, as expected (see Figure 2), and the sea-level temperature is consistent with mean annual temperatures for 50° South of approximately 15°C.

Table 1: Free Climate Parameters

Horizontal wind speed (m/s)	28.6329
Azimuth (degrees)	111.898
Sea-level temperature (°C)	15.039
Moist Brunt Väisälä frequency (rad/s)	0.000212366
τ (condensation and fall out times) (s)	668.634
Background precipitation (mm/hr)	1.47008

Table 1. Best-fit climate parameters determined from controlled random search and traditional least-squares, as defined in the text.

3.3 Model Output

Based on the equations detailed in sections 2.2-2.4 and the best-fit parameters described in 3.2, the model calculates the temperature, precipitation, reduced precipitation, drying ratio, hydrogen fractionation, and oxygen fractionation fields. The oxygen fractionation and drying ratio follow similar patterns to that seen in Figure 7 for hydrogen fractionation. As the amount of precipitation increases, the model demonstrates increasingly lighter isotopic composition for the precipitation. This indicates that the model is fundamentally working, fractionating over topography as desired.

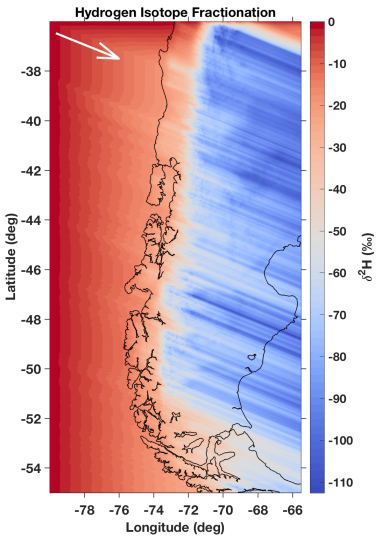

Figure 7. Hydrogen fractionation over the topography, as calculated by the model using the best-fit parameters. The δ^2H is initialized at a value of 0 and becomes increasingly depleted in heavy isotopes.

The model also calculates the predicted isotopic composition of a given geographical location from which there exists a sample. Notably, the correlations between predicted and observed values reach an R^2 value of 0.51, as seen in Figure 8 for hydrogen and oxygen. However, for relatively non-depleted samples, the predicted values tend to overestimate the fractionation of that sample, thus skewing the data towards a less-inclined slope than the desired one-to-one correlation.

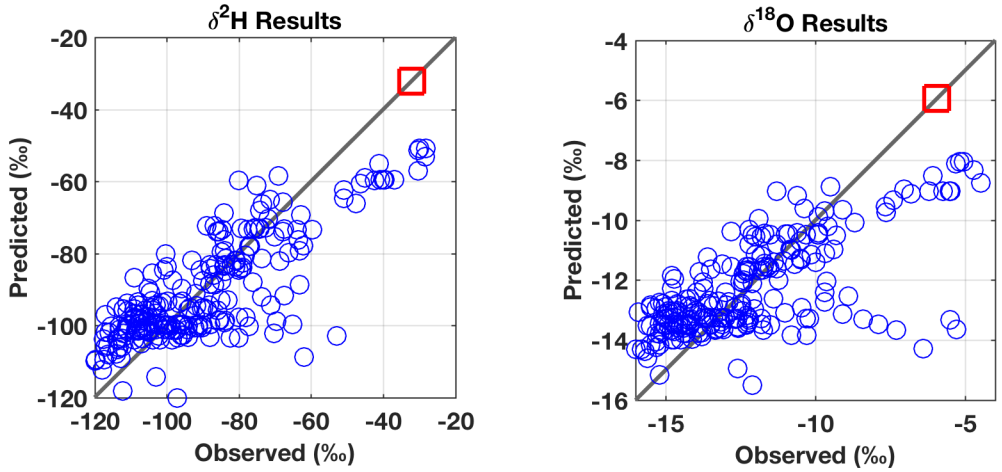

Figure 8. Predicted vs. observed isotopic ratios for hydrogen (left panel) and oxygen (right panel), with the one-to-one line marked in grey.

3.4 Complications

We note that in Figure 8, the model tends to further fractionate samples on the heavy end of the spectrum. In fact, analyzing the predicted isotopic data with respect to the global meteoric water line, it is evident that the slope of this predicted data is steeper than that of the global meteoric water line. As mentioned, the slope of the global line is 8, the data sampled is 8.11, and the model output is 9.32. This is illustrated in Figure 9, where the predicted δ^2H and $\delta^{18}O$ are plotted against each other.

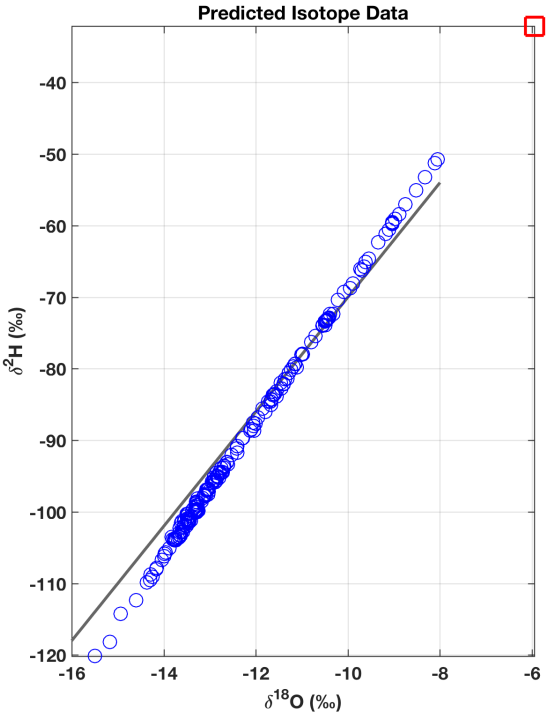

Figure 9. Predicted model data for δ^2H vs. $\delta^{18}O$ in comparison to the global meteoric water line (in grey).

In an attempt to explain this high slope value, we can examine the dependence between the slope ($\delta^2H/\ \delta^{18}O$) and the temperature, as the α values for both hydrogen and oxygen will be dependent on temperature and thus phase (Figure 10). Notably, for a slope of 8, the corresponding temperature is 36°C, whereas this study is concerned with values around 15°C, as shown in the model's best-fit estimate for sea level temperature. A slope of 9.32, as found for the predicted values, coincides with an estimated temperature of 3°C, far too cold for our study region. Therefore, while we do not have a conclusive reason for why the model is predicting more fractionation than actually present, it is evident that temperature could play an important role.

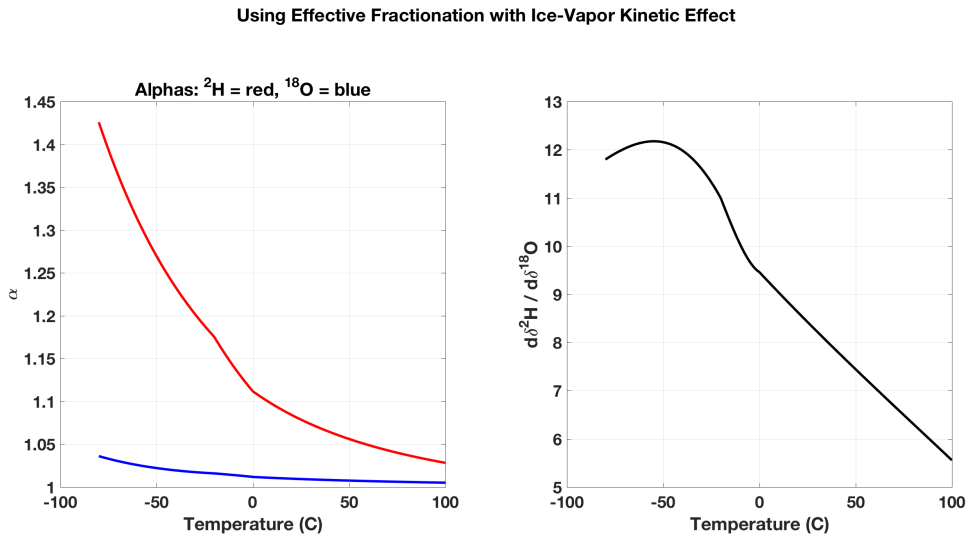

Figure 10. The α (fractionation factor) values for ^{2}H and ^{18}O and their dependence on temperature and therefore phase (Rowley and Garizone, 2007) (left panel). The slope of hydrogen to oxygen fractionation as a function of temperature (right panel).

4. Discussion and Summary

There are therefore three main messages to this analysis. Firstly, lifting and the associated precipitation are due primarily to three different mechanisms, only one of which depends on topography. Secondly, as moist stability, or the N_m value increases, it will depress the amount lifted and shift it upstream (i.e. exhibit blocking). However, this effect is offset as the larger the stability, the larger the characteristic height for moisture and therefore the more moisture in the atmosphere. Thirdly, fractionation is ultimately tied to the relative precipitation and drying ratio, which are relative measures. In other words, fractionation depends on relatives—not the magnitude of precipitation, but the amount of water lost relative to the total water vapor.

In addition, we have seen that the data is well-fit by the linear model and the physical parameters estimated by the model seem reasonable and consistent with other climatological values. However, we remain slightly skeptical of the anomalously high wind speed estimates, although Garreaud's data presented in Figure 2 provides affirmation for the value. In addition, we are still working on the explanation for the high result for the slope of the predicted isotopic values and how far from the GMWL these values are, while the observed data fits the GMWL well.

Acknowledgements

I would like express my deepest gratitude to Mark Brandon for the instruction, support, and mentorship throughout this study. In addition, I am grateful to David Auerbach for introducing me to the lab methods for volcanic glasses. I would also like to thank Professor Smith for the work that made this analysis possible.

References

Brown, J. W., and R. V. Churchill, 1993: Fourier Series and Boundary Value Problems, McGraw-Hill, Inc.

Clark, T.L., and W.R. Peltier, 1977: On the Evolution and Stability of Finite-Amplitude Mountain Waves. *Journal of the Atmospheric Sciences*, **34**, 1715-1730.

Craig, H., 1961: Isotopic Variations in Meteoric Waters: Science. *New Series*, **133**, 1702-1793.

Criss, R.E., 1999: Principles of Stable Isotope Distribution. *Oxford University Press*, 18 and 106-108.

Doyle, J.D., and Q. Jiang, 2006: Observations and numerical simulations of mountain waves in the presence of directional wind shear. *Quarterly Journal of the Royal Meteorological Society*, **132**, 1877-1905.

Durran, D.R., and J.B. Klemp, 1982: On the Effects of Moisture on the Brunt-Väisälä Frequency. *Journal of the Atmospheric Sciences*, **39**, 2152-2158.

Galewsky, J., 2009: Orographic precipitation isotopic ratios in stratified atmospheric flows: Implications for paleoelevation studies. *Geology*, **37**, 791-794.

Garreaud, R, 2016, The Climate of Patagonia: Glaciers, Flashes and Shadows. Presentation to Yale G&G department, 4-26-2016.

Garreaud R., P. Lopez, M. Minvielle, and M. Rojas, 2013: Large-Scale Control on the Patagonian Climate. *Journal of Climate*, **26**, 215-230.

Hansen, P.C., V. Pereyra, and G. Scherer, 2012: Least Squares Data Fitting with Applications. JHU Press.

Horita, J., and D. Wesolowski, 1994, Liquid-vapor fractionation of oxygen and hydrogen isotopes of water from the freezing to the critical temperature. *Geochimica et Cosmochimica Acta*, **58**, 3425-3437.

Jouzel, J., and L. Merlivat, 1984: Deuterium and Oxygen 18 in Precipitation: Modeling of the Isotopic Effects During Snow Formation. *Journal of Geophysical Research*, **89**, 11749-11757.

Lin, Y., 2007: Mesoscale Dynamics. Cambridge University Press, p 14-16.

Lindeman, J., D. Broutman, S.D. Eckermann, J. Ma, and Z. Boybeyi, 2010: A coupled mesoscale-model Fourier-method for idealized mountain-wave simulations over Hawaii. *Meteorology and Atmospheric Physics*, **108**, 71-81.

Nappo, C.J., 2002: An Introduction to Atmospheric Gravity Waves. Academic Press, p 66-67.

Poage, M.A., and C.P. Chamberlain, 2001: Empirical Relationships between elevation and the stable isotope composition of precipitation and surface waters: considerations for studies of paleoelevation change. *American Journal of Science*, **301**, 1-15.

Rowley, D.B., 2001: A new approach to stable isotope-based paleoaltrimetry: implications for paleoaltimetry and paleohysometry of the High Himalaya since the Late Miocene. *Earth and Planetary Science Letters*, **188**, 253-268.

Rowley, D.B., and C.N. Garzione, 2007: Stable Isotope-Based Paleoaltimetry: *Annual Review of Earth and Planetary Sciences*. **35**, 463-508.

Smith, R.B. and I. Barstad, 2004: A Linear Theory of Orographic Precipitation. *Journal of the Atmospheric Sciences*, **61**, 1377-1391.

Smith, R.B., S. Skubis, J.D. Doyle, A.S. Broad, C.K. Kiemle, and H. Volkert, 2002: Mountain Waves over Mont Blanc: Influence of a Stagnant Boundary Layer. *Journal of Atmospheric Sciences*, **59**, 2073-2092.

Smith, R.B., I. Barstad, and L. Bonneau, 2005: Orographic Precipitation and Oregon's Climate Transition: *Journal of Atmospheric Sciences*, **62**, 177-191.

Smith, R.B., and J.P. Evans, 2007: Orographic precipitation and water vapor fractionation over the southern Andes. *Journal of Hydrometeor*, **8**, 3-19.

Smith, R.B., 1979: The influence of mountains on the atmosphere. *Advances in Geophysics*, **21**.

Smith, R.B., 1980: Linear theory of stratified hydrostatic flow past an isolated mountain. *Tellus*, **32**, 348-364.

Smith, R.B., 1989: Hydrostatic airflow over Mountains. *Advances in Geophysics*, **31**, 1-41.

Smith, R.B., 2003: Advection, diffusion, and deposition from distributed sources: *Boundary Layer Meteorology*, **107**, 273-287.

Smith, R.B., 2006: Progress on the theory of orographic precipitation. *Geological Society of America Special Papers*. ***398***, 1-6.

Smith, R.B., 2007: A linear upslope-time-delay model for orographic precipitation. *Journal of Hydrology*, **282**, 2-9.

Stern, L.A., and P.M. Blisniuk, 2002: Stable isotope composition of precipitation across the southern Patagonian Andes. *Journal of Geophysical Research*, **207**, ACL3-1-ACL3-14.

Wallace, J.M., and P.V. Hobbs, 2006: Atmospheric Science: An Introductory Survey. Academic Press.

Appendix: Data

Sample	Latitude	Longitude	Obs Elev (m)	δ18O (‰)	δD (‰)
15SW01	-45.68473	-72.05653	360	-10.7	-81
15SW02	-45.68473	-72.05653	360	-13.1	-93
15SW03	-45.80654	-71.92004	416	-13.5	-100
15SW04	-45.96938	-71.86899	930	-14.4	-106
15SW05	-46.16361	-72.6368	527	-12.4	-87
15SW06	-46.42736	-72.70784	214	-11.3	-81
15SW07	-46.82204	-72.66509	214	-14.2	-104
15SW08	-46.54557	-71.79084	379	-14.2	-108
15SW09	-46.72698	-71.73816	552	-14.6	-112
15SW10	-46.78768	-71.911	723	-15.1	-111
15SW100	-47.49968	-72.9548	85	-14.3	-104
15SW101	-48.00343	-73.5806	7	-11.3	-80
15SW102	-47.91925	-73.88113	0	-9.5	-69
15SW103	-48.15612	-73.54459	0	-10.6	-75
15SW11	-46.80099	-71.94523	791	-15.2	-113
15SW12	-46.81897	-71.98706	836	-14.7	-108
15SW13	-46.83839	-72.01135	847	-14.2	-105
15SW14	-46.83762	-72.01592	869	-15.6	-116
15SW15	-46.70704	-71.70413	487	-15.5	-117
15SW16	-46.60542	-71.69001	338	-13.9	-107
15SW17	-46.54565	-71.79073	372	-14.2	-111
15SW18	-46.55434	-71.89324	408	-15.9	-117
15SW19	-46.56208	-72.02654	474	-15.5	-114
15SW20	-46.5905	-72.22621	247	-14.8	-105
15SW21	-46.62461	-72.3532	437	-14.7	-109
15SW22	-46.69712	-72.43269	300	-14.8	-104
15SW23	-46.83948	-72.69064	226	-12.7	-94
15SW24	-46.79345	-72.58239	367	-14.6	-103
15SW25	-46.79217	-72.57853	385	-15.1	-108
15SW26	-46.99745	-72.79652	393	-15.1	-109
15SW27	-47.12106	-72.77589	192	-12.1	-85
15SW28	-47.12755	-72.70493	176	-14.8	-108
15SW29	-47.12701	-72.48109	459	-14.8	-109
15SW30	-47.14937	-72.46811	878	-15.3	-111
15SW31	-47.15234	-72.508	1156	-14.1	-104
15SW32	-47.15315	-72.52048	1060	-15.5	-112
15SW33	-47.14729	-72.52844	773	-15.0	-109
15SW34	-47.11804	-72.46352	439	-9.1	-78
15SW35	-47.12104	-72.4628	451	-14.1	-105
15SW36	-47.06494	-72.35657	485	-5.0	-55

15SW37	-47.06477	-72.35623	486	-12.8	-100
15SW38	-47.12766	-72.50525	391	-14.9	-109
15SW39	-46.79156	-72.81326	221	-15.2	-111
15SW40	-46.72605	-72.80261	261	-14.0	-98
15SW41	-45.53469	-72.72427	237	-12.8	-89
15SW42	-46.4579	-72.72153	208	-12.3	-84
15SW43	-46.35799	-72.76529	234	-11.9	-80
15SW44	-46.4579	-72.72153	208	-12.2	-82
15SW45	-46.1715	-72.71604	587	-11.6	-79
15SW46	-46.4579	-72.72153	208	-12.8	-88
15SW47	-46.15901	-72.33672	310	-13.0	-92
15SW48	-46.10975	-72.11713	501	-14.9	-109
15SW49	-46.0595	-72.00636	1030	-14.7	-106
15SW50	-45.988	-71.90952	853	-14.6	-106
14AR03	-45.46989	-69.83440	411	-10.8	-80
14AR04	-46.58285	-70.91703	394	-13.4	-102
14AR05	-47.07494	-70.83244	659	-12.6	-103
14AR06	-46.55421	-71.63984	232	-14.9	-113
14CL01	-46.82732	-72.00060	839	-14.2	-105
14CL02	-47.12105	-72.77598	195	-11.4	-83
14CL03	-47.12801	-72.50515	375	-14.0	-103
14CL04	-46.19178	-72.77643	539	-11.7	-79
14LP80	-47.59016	-71.82466	1017	-14.5	-117
AldeaEscolar	-43.13293	-71.55641	350	-12.03	-85.87
Andrade1	-45.15287	-73.51875	22	-5.49	-39.46
Andrade2	-45.15290	-73.51875	22	-5.52	-40.81
Andrade3	-45.15290	-73.51875	22	-5.74	-39.87
Andrade4	-45.15290	-73.51875	22	-5.5	-36.91
Arr. Fontana	-42.99002	-71.56104	633	-12.24	-83.96
Arr. Raninto	-42.95405	-71.59155	599	-12.29	-85.51
Arr.Aserradeo	-46.17085	-72.68223	548	-12.34	-83.74
Arr.Lepa	-42.61490	-71.07693	836	-12.66	-95.51
Arr.Montoso	-42.74054	-71.09752	982	-13.14	-95.46
ArrPedegoso	-46.62000	-71.26723	247	-12.57	-105.95
Cascada Tio Mindo	-42.83907	-71.60286	569	-12.47	-90.40
CerroCastillo	-46.93263	-72.34239	697	-13.92	-100.36
CerroJeinemeni	-46.71988	-72.45667	251	-13.74	-98.28
CerroPicoSur	-46.54514	-71.78318	354	-13.16	-103.89
CerroSinNombre	-46.12166	-72.54284	353	-12.43	-87.99
Chaiten1	-42.88976	-72.74016	48	-6.8	-46.37
Darwin	-41.88169	-73.66249	10	-5.31	-30.27
EastLake	-40.08755	-71.18360	782	-12.26	-92.36

Escalera	-41.30213	-71.49230	799	-13.34	-96.98
Farm Pond	-40.60503	-72.89162	94	-7.4	-50.85
GauchitaGil	-46.60238	-71.17864	274	-13.09	-107.4
Guillermo	-41.43908	-71.48543	900	-13.07	-94.13
La Parra	-46.72985	-72.79275	242	-13.53	-101.11
Las Chilcas	-46.61174	-71.33814	235	-13.32	-107.76
Las Pizarras	-45.46967	-72.30587	101	-10	-68.67
Leleque	-42.43053	-71.10339	726	-13.61	-98.82
Los Antiguos	-46.55461	-71.63969	227	-14.55	-115.44
MechaicoPnte	-41.93832	-73.83016	6	-5.05	-28.11
MiradordelRio	-43.97448	-72.46558	37	-10.37	-71.37
MurrowPnte	-41.66290	-73.31739	26	-4.72	-28.28
Nahuelhuapi	-40.94165	-71.36930	822	-11.75	-88.09
Pnte Arauca	-43.30735	-72.41812	252	-9.93	-67.80
Pnte Viviana	-45.35084	-72.46155	45	-11.06	-83.65
Pnte. El Salto	-45.44705	-72.78023	11	-8.68	-62.74
Pnte. Prieto	-45.43151	-72.72117	17	-9.59	-71.8
PnteLoicas	-43.52608	-72.34195	165	-9.67	-66.23
PnteNique	-40.72393	-72.43294	203	-7.63	-47.46
PntePedregoso	-45.08365	-72.11827	257	-11.77	-79.31
Pt Bertrand	-46.94433	-72.78630	226	-14.3	-103.78
Pte Catalan	-46.99686	-72.79647	393	-13.81	-102.08
Pte Leonos	-46.73664	-72.85837	248	-12.97	-93.58
Pte. Moro	-45.50075	-72.15421	135	-11.53	-84.14
Pte. Rossel	-45.42446	-72.41638	73	-10.13	-63.14
PteBlas	-46.62462	-72.67262	218	-12.28	-90.77
PteChirito	-46.62461	-72.67262	219	-13.88	-100.81
PteSantaMarta	-46.72628	-72.80218	226	-13.23	-96.59
PuertoArauca	-40.72533	-71.68749	794	-11.01	-79.95
PuertoMontt	-41.47001	-72.93515	37	-7.04	-45.06
PuertoMurta	-46.37869	-72.74555	250	-12.26	-87.77
PulchicanPnte	-41.96151	-73.83674	0	-5.19	-29.87
Rio Aviles	-46.59066	-72.22546	254	-13.72	-95.82
Rio Bana	-46.55488	-71.89392	423	-14.68	-107.44
Rio Jeinemeni	-46.58089	-71.66023	258	-14.16	-107.25
Rio Senguer	-45.47014	-69.83080	413	-10.29	-82.40
Rio Totoral	-40.71230	-71.78998	779	-9.69	-71.24
RioButalcuva	-42.27947	-73.70856	62	-6.09	-41.16
RioCisnes	-44.69370	-72.24080	194	-10.84	-76.92
RioDeseguardero	-42.88937	-71.60884	518	-12.48	-88.76
RioEngano	-46.45846	-72.72255	222	-11.72	-86.49
RioFoyal	-41.72230	-71.45573	672	-12.44	-92.16
RioManihuales	-45.29296	-72.32626	96	-11.22	-84.82

RioMayo	-45.68462	-70.25097	420	-10.45	-89.88
RioPireco	-40.73363	-71.83179	804	-9.69	-67.51
RioPuychue	-40.72516	-71.92764	1154	-9.63	-63.1
RioSimpson	-45.47912	-72.28231	117	-11.37	-80.67
RioTrapial	-46.70510	-72.69632	312	-13.97	-104.52
Sta Barbara	-42.85573	-72.79425	16	-6.2	-42.33
Sta.Andres	-44.88360	-72.20406	349	-10.48	-73.6
Trapen Pnte	-41.52285	-73.09121	68	-4.48	-30.33
Waterfall Seno	-44.50999	-72.55828	3	-7.67	-50.93
G3-01	-47.56708	-72.86353	90	-13.6	
P3-00-1	-47.68212	-73.02468	68	-13.6	-100.3
P3-00-2	-47.76640	-73.26593	48	-10.3	-67.4
PASW00-1	-47.67240	-71.77578	1800	-15.2	-112.2
PASW00-2	-47.58833	-71.82500	940	-14.1	-116.2
PASW1	-47.77800	-73.29790	45	-10.6	-72.5
PASW10	-47.56727	-72.86360	90	-14.2	-95.7
PASW11	-47.12097	-72.04780	590	-14.3	-101.8
PASW12	-47.16085	-71.83540	630	-15.3	-113.6
PASW13	-47.74343	-71.19690	851	-6.4	-62.0
PASW14	-47.63388	-71.27680	860	-15.3	-117.6
PASW15	-47.44500	-72.06438	475	-13.9	-96.1
PASW16	-47.43510	-72.03600	490	-14.8	-106.6
PASW17	-47.43367	-72.01890	450	-14.4	-102.2
PASW18	-47.42713	-72.00170	410	-14.5	-108.7
PASW19	-47.42028	-71.94320	167	-15.0	-105.4
PASW2	-47.76750	-73.27250	45	-11.0	-76.0
PASW20	-47.45858	-71.86050	170	-8.4	-69.6
PASW21	-47.45538	-71.81250	160	-10.2	-83.8
PASW22	-47.83268	-71.29620	849	-12.1	-97.1
PASW23	-47.57563	-71.38190	625	-15.0	-111.3
PASW24	-47.63293	-71.74480	1225	-15.7	-119.9
PASW25	-47.64838	-71.74240	1520	-15.6	-117.8
PASW26	-47.83237	-72.12690	866	-13.5	-99.6
PASW27	-47.83237	-72.12690	866	-12.3	-94.2
PASW28	-47.71393	-72.15320	895	-16.0	-119.7
PASW29	-47.71393	-72.15320	895	-15.8	-117.3
PASW3	-47.76693	-73.26990	45	-10.9	-74.4
PASW30	-47.70938	-72.16670	973	-15.3	-112.7
PASW31	-47.80372	-72.00780	933	-15.2	-114.0
PASW32	-47.81683	-72.01810	961	-14.8	-113.2
PASW33	-47.76788	-72.22130	961	-14.7	-106.9
PASW34	-47.76772	-72.21220	906	-15.1	-109.0
PASW35	-47.76835	-72.08800	995	-15.5	-116.3

PASW36	-47.80345	-72.08420	850	-13.8	-107.1
PASW37	-47.94937	-72.13460	918	-12.7	-91.2
PASW38	-47.94855	-72.14040	910	-12.6	-94.0
PASW39	-47.95075	-72.14570	910	-13.0	-95.6
PASW4	-47.76653	-73.26490	48	-11.0	-74.1
PASW40	-47.95372	-72.15740	916	-13.6	-102.3
PASW41	-47.95217	-72.14800	895	-13.6	-100.9
PASW42	-47.94857	-72.13350	898	-13.6	-99.8
PASW43	-47.95043	-72.12120	892	-13.7	-97.3
PASW44	-47.95583	-72.11060	890	-13.4	-96.4
PASW45	-47.94315	-72.08300	890	-11.8	-87.8
PASW46	-47.93808	-72.05980	860	-12.2	-89.9
PASW47	-47.94305	-71.88300	878	-14.3	-100.9
PASW48	-47.99138	-71.81980	844	-13.5	-98.5
PASW49	-47.57547	-71.56310	290	-12.6	-97.3
PASW5	-47.73647	-73.23540	15	-12.0	-85.5
PASW50	-47.57058	-71.58380	245	-12.3	-91.3
PASW51	-47.57403	-71.62010	190	-11.5	-90.1
PASW52	-47.77238	-73.28810	45	-11.7	-79.3
PASW53	-47.76338	-73.25740	45	-11.5	-77.6
PASW54	-47.75738	-73.24570	45	-9.9	-63.9
PASW55	-47.74817	-73.23990	38	-9.3	-59.6
PASW56	-47.72333	-73.20340	23	-10.5	-70.1
PASW57	-47.72217	-73.17270	7	-11.3	-63.6
PASW58	-47.69807	-73.12540	40	-9.4	-62.1
PASW59	-47.69668	-73.04615	25	-12.0	-84.0
PASW6	-47.73647	-73.23540	3	-12.1	
PASW60	-47.68987	-73.03530	43	-11.8	-84.8
PASW61	-47.67335	-73.01470	35	-10.5	-78.3
PASW62	-47.60977	-72.90540	138	-12.5	-76.1
PASW63	-47.54703	-72.86080	90	-12.9	-88.2
PASW64	-47.51350	-72.86530	93	-13.6	-91.8
PASW65	-47.31165	-72.59630	291	-8.9	-73.6
PASW66	-47.12102	-72.04830	538	-13.9	-98.5
PASW67	-47.52348	-71.80300	160	-14.2	-107.9
PASW68	-47.45490	-71.81290	160	-10.3	-85.3
PASW69	-47.58983	-71.74620	220	-15.2	-113.7
PASW7	-47.72177	-73.17180	7	-12.2	-84.1
PASW70	-47.57783	-71.73490	180	-7.3	-70.3
PASW71	-47.57888	-71.28350	624	-14.3	-106.9
PASW72	-47.56968	-71.63590	190	-7.9	-77.2
PASW8	-47.70315	-73.10340	28	-10.8	-77.2
PASW9	-47.60990	-72.87710	95	-12.1	-86.7

PASW99-1	-47.55265	-71.86100	940	-13.8	-112.4
PASW99-10	-47.76660	-73.26523	48	-12.1	-84.6
PASW99-11	-47.73568	-73.23563	5	-11.8	-86.1
PASW99-12	-47.56727	-72.86363	90	-14.2	-99.8
PASW99-13	-47.61105	-72.91417	120	-12.4	-89.9
PASW99-14	-47.05633	-72.26918	365	-5.3	-52.8
PASW99-15	-47.12122	-72.04712	556	-14.3	-103.9
PASW99-2	-47.55465	-71.86747	1105	-14.4	-113.4
PASW99-3	-47.17647	-71.82153	630	-14.7	-112.3
PASW99-4	-47.91857	-73.33020	60	-9.1	-67.8
PASW99-5	-47.91445	-73.32555	80	-9.7	-73.4
PASW99-6	-47.89535	-73.31915	95	-9.9	-74.1
PASW99-7	-47.88635	-73.31773	245	-11.9	-84.1
PASW99-8	-47.85225	-73.30232	320	-12.2	-86.7
PASW99-9	-47.78310	-73.30697	125	-9.9	-75.5
PV2-01	-47.76658	-73.26397	7	-10.6	
PX1	-47.95008	-72.13430	918	-13.2	-102.4
PX2	-47.95330	-72.15757	916	-14.7	-110.6
PX3	-47.95223	-72.14850	895	-13.4	-100.1
PX4	-47.83273	-72.12607	866	-13.1	-102.9
PX5	-47.83273	-72.12607	866	-11.8	-97.5
PX6	-47.92920	-72.04543	890	-5.5	-65.1